# Controllable Spin-Split Phantom Scars in Quantum Dots

*Michael Berger\* and Jamal Berakdar\**

Quantum states of systems with an underlying classical chaotic dynamics can be "scarred," meaning that the associated probability density is localized around the short, unstable periodic orbits. Here, it is shown that, via tunneling, the scarred state can be imaged to a region that does not support scarring. This "phantom scar" is also present in the spin channel and has marked influence on the spin-dependent system dynamics, as illustrated by explicit calculations for the fidelity and correlation functions. Numerical simulations and analysis are performed for the spin-dependent electron dynamics in semiconductor-based double quantum dots, including disorder, Rashba-type spin-orbital coupling, exchange fields, and external magnetic fields. The results elucidate the unique feature of scarring as a coherent phenomenon spanning the whole system and affecting its localization properties in a narrow spectral window.

## 1. Introduction

Waves representing classical and quantum particles moving in space with complex boundaries have been discussed widely for a variety of systems such as classical (quantum) billiards or microwave resonators.[1–7] Particularly interesting is the issue of classical-quantum crossover behavior. For quantum systems with underlying classical integrable behavior, the Bohr–Sommerfeld quantization procedure provides an insight into the quantum dynamics based on classical periodic orbits. Considering the quantum dynamics of a classically chaotic system (e. g., Bunimovich stadium), it has been observed that short-term, unstable periodic orbits[7–9] leave footprints in the spatial texture of the wavefunctions. As put by Heller,[7] "They induce *scars* of larger than expected density in at least some of the wave functions."[10,11] The scarring-enhanced localization of the probability density and how it shows up in physical observables have been investigated theoretically and experimentally[12] for a number of settings.[13–27]

M. Berger, J. Berakdar
Martin-Luther Universität Halle-Wittenberg, Institut für Physik
06099 Halle, Germany
E-mail: michael.berger@physik.uni-halle.de; jamal.berakdar@physik.uni-halle.de

While in billiard systems the characteristics of periodic orbits are sensitive to the boundary geometry (in the quantum case, Dirichlet boundary conditions are usually imposed), introducing finite-size random impurities may render (an otherwise integrable) dynamics chaotic, in which case scars are observed[20,28,29] and disappear in the absence of impurity scattering. Hence, boundary induced scars are referred to as geometrical scars, and impurity-induced ones are called dynamical scars. Classical many-body interacting systems are generically chaotic, raising the question of many-body quantum scarring when varying the interparticle interaction strength, an issue that is currently under investigation[30–34] and is distinct from many-body localization in disordered quantum systems.[35–42]

For dynamical scarring, studies were mainly focused on scalar impurities or spin-independent interparticle interactions. Here, we consider dynamical scarring in confined electronic systems with non-trivial spin dynamics. Generally, one may have scattering in the spin channel only (for instance, scattering from a magnetic domain wall[43]) and yet act on the charge channel. For a system hosting a spin-orbital coupling, scalar impurity scattering can lead to spin-dependent scarring[44] and mix the spin channels for a magnetic system. Another aspect to be addressed here is the possibility of teleportation of scarred states (as quantified below) to a localized region which for itself does not exhibit scarring. To this end, we study a fairly general model that can be realized on the basis of exchanged split, spin-dependent 2D electron gas (2DEG) confined to two coupled quantum dots (QDs) hosting a spin orbital coupling of the Rashba type. Impurities can be dispersed over the whole system or only in one of the dots. We calculate a large number of single-particle states sufficient to quantify the appearance and the spectral properties of spin-dependent scars and visualize them. It is found that at energies above the tunneling barrier between the QDs, scars also appear in the region without impurities. Even for energies below the tunneling barrier, and even if the isolated QD without impurities does not exhibit any scars, tunneling scars appear as the image of those formed in the dots with impurities. The influence of the results on the revival probability is illustrated with full numerical time propagation.

The rest of the paper is organized as follows. In Section 2.1 we introduce the theoretical model and numerical tools. The statistical methods are in Section 2.2. Results for various system parameters are presented and discussed in Section 3, followed by a summary in Section 4.

**ADVANCED
SCIENCE NEWS**

www.advancedsciencenews.com

**ADVANCED
QUANTUM
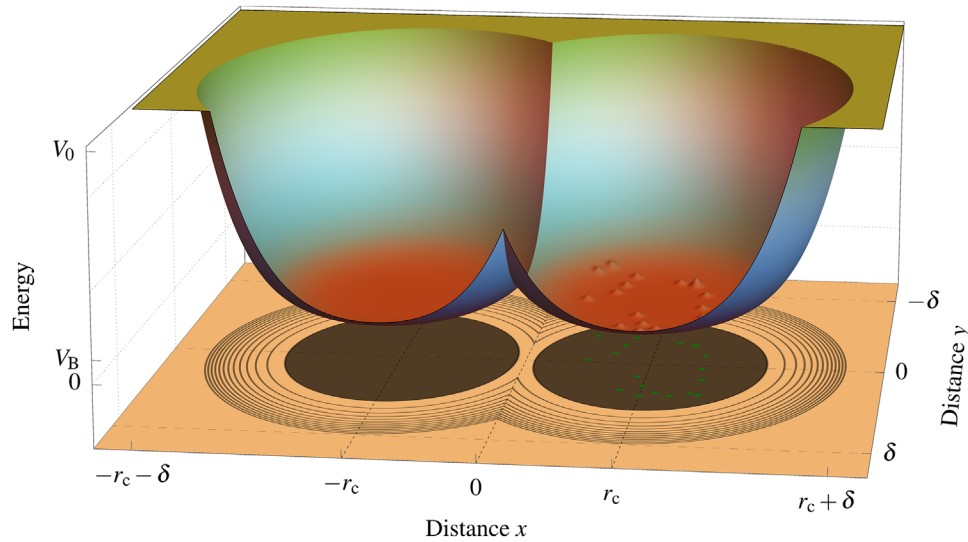TECHNOLOGIES**

www.advquantumtech.com

**Figure 1.** Cross-section of the double quantum dots potential confining the motion in the $x$–$y$ plane. The centers of the QDs are shifted by a distance $\pm r_c$ along the $x$-axis. The potential upper value $V_0 = 68.5$ meV is reached at $x = r_c + \delta$. $V_B$ indicates the top of the tunneling barrier height between the QDs. The green dots in contour plot indicate the locations of the impurities (bumps) in the right QD.

## 2. Model and Methods

### 2.1. Hamiltonian

We study the spin-dependent quantum dynamics of charge carriers in coupled QDs in an external magnetic field. An exchange field may be present (rendering the system magnetic) as well as spin-orbital interaction. The carriers scatter elastically from $N_{\text{Imp}}$ localized scalar impurities. The aim is to trace the emergence and stability of the spin-dependent quantum scars and the possibility of quantum tunneling of the formed scars to a region that otherwise does not host any scars.

The Hamiltonian of this setting reads

$$\mathcal{H} = \frac{\Pi^2}{2m^*} + \alpha(\boldsymbol{\sigma} \times \boldsymbol{\Pi})_z + V(\boldsymbol{r}) + \sum_{n=1}^{N_{\text{Imp}}} V_{\text{Imp}}(\boldsymbol{r}, \boldsymbol{r}_n) + \frac{1}{2} g \mu_B B_0 \sigma_z$$
$$+ H_{\text{Ex}}(\boldsymbol{r}) \cdot \boldsymbol{\sigma} \tag{1}$$

where $\boldsymbol{\Pi} = \boldsymbol{p} - e\boldsymbol{A}(\boldsymbol{r})$ is the momentum in the electromagnetic fields described by the vector potential $\boldsymbol{A}(\boldsymbol{r})$ associated with a static, homogeneous external magnetic field $B_0 \boldsymbol{e}_z$ applied perpendicularly (along $\boldsymbol{e}_z$) to the QDs. $m^*$ is the effective electron mass. $V(\boldsymbol{r})$ is the potential restricting the motion to be described here to a region in the $x$–$y$ plane. $V_{\text{Imp}}$ is the impurity potential (cf. **Figure 1**). $\alpha$ is the Rashba spin-orbit coupling strength. Additionally, an effective (exchange) field $H_{\text{Ex}}(\boldsymbol{r})$ is included as to capture the spin-polarization for the magnetic case.[45] $\boldsymbol{\sigma}$ is the vector of the Pauli matrices. We assume the dot to the right to be magnetic. Unless otherwise stated, the effective mass $m^*$ is set to unity. We consider Gaussian impurities (the bumps within the right dot in Figure 1) of the form

$$V_{\text{Imp}}(\boldsymbol{r}, \boldsymbol{r}_n) = M \exp\left\{ -\frac{(\boldsymbol{r} - \boldsymbol{r}_n)^2}{2\sigma^2} \right\} \tag{2}$$

The parameters $M$ and $\sigma$ define the strength and width of an impurity, respectively. For the sake of simplicity, all impurities have the same shape. We studied the cases where the confining potential $V(\boldsymbol{r})$ is a harmonic ($V \propto r^2$) potential for the left dot (linear system) coupled to $r^5$ potential for the right dot (nonlinear system) and where both dots are described by $r^5$ potentials. The choice of the $r^5$ potential is to connect with previous studies in some limiting cases[28,46] (i.e., for one spin-independent dot). An electron in a single spin-independent $r^5$ potential is found to have states with star-shaped scars with five, seven, or more corners.[28,46] Those patterns are found throughout the whole eigenfunction spectrum, while the scarred fraction depends on the number, width, and strength of the impurities, which break the rotational symmetry. In the limit of strong perturbation ($M \gg 1$), the scars vanish and the wave functions exhibit a chaotic behavior. We reproduced these observations (in the limits $\alpha = 0$, $B_0 = 0$, $H_{\text{Ex}} = 0$, and only one dot).

For brevity, below we present results for the confining potential shown in Figure 1. Each QD is radially symmetric around a center point $\pm r_c$, the centers are separated by a distance $w = 2r_c$. The potential $V_0$ sets the escape energy of the electron from the QDs. Mathematically the confinement is described by

$$V(\boldsymbol{r}) = \text{Min}\left\{ \frac{1}{2}(\boldsymbol{r} - \boldsymbol{r}_c)^5, \frac{1}{2}(\boldsymbol{r} + \boldsymbol{r}_c)^5, V_0 \right\}, \quad r(x,y) = \sqrt{x^2 + y^2},$$
$$\boldsymbol{r}_c = r_c \boldsymbol{e}_x \tag{3}$$

The eigenstates analyzed below are energetically well below $V_0$. Changing the parameter $r_c$ moves the dots toward or away from each other along the $x$-axis, while preserving symmetry. Therefore, in the overlapping region an effective tunnel barrier is created for states with energies in the range of and below $V_B$ (cf. Figure 1). The sharp value in the potential at $x = 0$ can be locally Gaussian smoothed (with no observable effects on the results).

To quantify and illustrate the degree of localization, we calculate for a given eigenstate energy $E_i$ the eigenstates $\Psi_{\alpha, E_i}(x, y)$

**ADVANCED
SCIENCE NEWS**

www.advancedsciencenews.com

**ADVANCED
QUANTUM
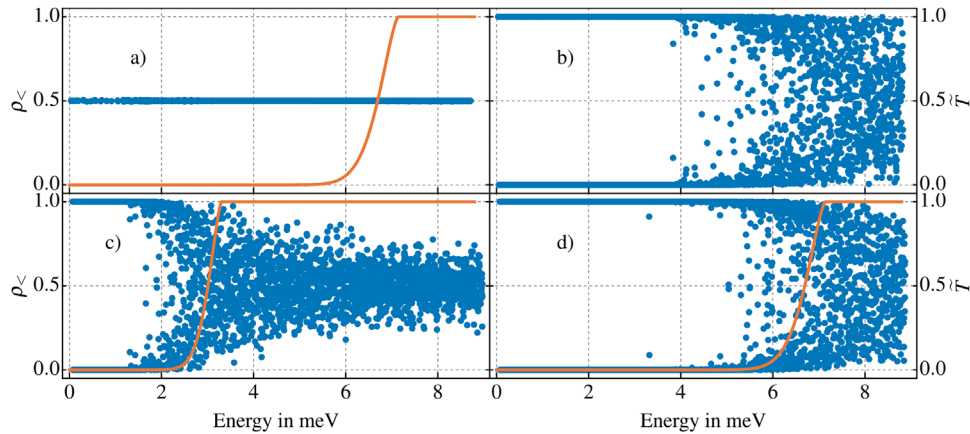TECHNOLOGIES**

www.advquantumtech.com

**Figure 2.** Partial probability densities $\rho_<$ (as defined by Equation (4)) in the left QD as the eigenstate energy increases starting from the ground state. Distance between the QDs centers is $w = 318$ nm. Impurities reside in the right QD and have a width of $\sigma = 5.3$ nm (cf. Equation (2)). We consider $N_{\mathrm{Imp}} = 261$ independent impurities. The orange lines indicate the tunneling probability ($\tilde{T}$) for a state of given energy in WKB approximation along $y = 0$ (cf. Equation (5)). Top row: Impurity strength is $M = 0$ in (a) or $M = 0.4$ meV in (b). When the eigenenergy is large enough (with respect the top of the tunneling barrier), the wave functions tunnels and spreads evenly over the whole system, hence, the partial densities are equal, $\rho_< = \rho_> = 0.5$. Adding impurities the left/right symmetry is broken. Bottom row: Impurity strength is fixed at $M = 0.54$ meV and the QDs centers are shifted by c) 160 nm and d) 185 nm. In comparison with panels (a,b), wave functions can localize in either QDs even when energetically, the tunneling barrier is surpassed.

where $\alpha$ designates all other good quantum numbers beside $E_i$ (the dynamics along the $z$-direction is assumed to be frozen by appropriately strong confinement). The probability density in the left ($\rho_{x<0}$) and the right ($\rho_{x>0}$) QD (the impurities are elastic and no environmental coupling is present) read

$$\rho_< = \int_{-\infty}^{\infty} \mathrm{d}y \int_{-\infty}^{x=0} \mathrm{d}x \frac{1}{|\kappa|} \sum_{\kappa} \left| \Psi_{\kappa, E_i}(x, y) \right|^2, \rho_> = 1 - \rho_< \tag{4}$$

where $\kappa$ counts degenerate states at energy $E_i$ and $|\kappa|$ is the number of degenerate states.

Due to symmetry in absence of impurities, the electron is equally likely to reside in either of the dots (**Figure 2**). The left/right symmetry is broken when adding impurities and the states localize either to the left or right QD in the low-energy regime (see Figure 2b). With increasing $E_i$, the wave function penetrates the tunnel barrier. In the limit, where the eigenenergy is in the range of $V_B$ or higher, the states delocalize over both QDs but partial densities are not necessarily equal. Our findings are supported by the semi-classical tunneling probability. We define the WKB approximation along the line at $y = 0$, reading

$$\tilde{T}(E) = \exp\left( -2 \int_{-x_B}^{x_B} \sqrt{\frac{2m^*(V(xe_x) - E)}{\hbar^2}} \mathrm{d}x \right) \tag{5}$$

$x_B$ denotes the turning point of the classical trajectory, that is, the point at which $E = V(\mathbf{r})$. The examples $\rho_<$ in Figure 2 are displayed for 3000 eigenstates with maximum energies of $E_{\max} \simeq 9$ meV alongside with the WKB approximation (Equation (5)). In Figure 2a, $r_c = 185$ nm and no impurities are added, therefore $\rho_< = 1/2 = \rho_>$. Panel 2b shows the partial densities with impurities (with $M = 0.4$ meV, $\sigma = 5.3$ nm) residing in the right QD which result in localization on either of the dots. The influence of the distance between the QDs on the partial densities is shown in Figure 2c,d. In Figure 2c $r_c = 160$ nm and in Fig-

ure 2d $r_c = 185$ nm and impurities are placed on the right side of the system in both cases ($M = 0.54$ meV, $\sigma = 5.3$ nm). The barrier heights are $V_B = 3.3$ and 7.2 meV, respectively. The first 500 states for $r_c = 160$ nm can be considered to be *independent*, when the impurities are added (Figure 2c). In a single electron picture, the probability to find the particle on either side of the double potential is one. Increasing the distance $w$ to 370 nm, the transition region between coupled (via tunneling) and uncoupled regions broadens and the first 1500 states may be considered to be uncoupled (Figure 2d). In Figure 2d the impurities are 30% stronger with respect to Figure 2b, otherwise the setup is the same. Evidently, the overall measure of the coupling in this sense does not depend on the particular perturbation. Already impurities with $M = 54$ μeV render similar results.

## 2.2. Quantifying Scarring

### 2.2.1. Statistical Measures

Scars for a single QD are well studied,[28] and the dependence of multiple statistical parameters on the impurity parameters was investigated previously.[20] We use statistical measures to judge chaoticity. Statistics however is not a sufficient indicator for scarring, as detailed below. Therefore, the energy spectrum is usually analyzed with further tools,[20,47–49] where multiple statistical parameters are introduced to have a quantitative measure for chaoticity. Of a particular interest are the distances of consecutive energy levels, that is, the distribution of the nearest neighbor level spacings (NNLS). A common tool is the *Brody*-distribution $p_\nu(s)$[50] for NNLS $s$, given by

$$p_\nu(s) = a_\nu(\nu + 1)s^\nu \exp\left(-a_\nu s^{\nu+1}\right),$$

$$a_\nu = \Gamma\left(\frac{\nu + 2}{\nu + 1}\right)^{\nu+1} \tag{6}$$

**ADVANCED
SCIENCE NEWS**

www.advancedsciencenews.com

**ADVANCED
QUANTUM
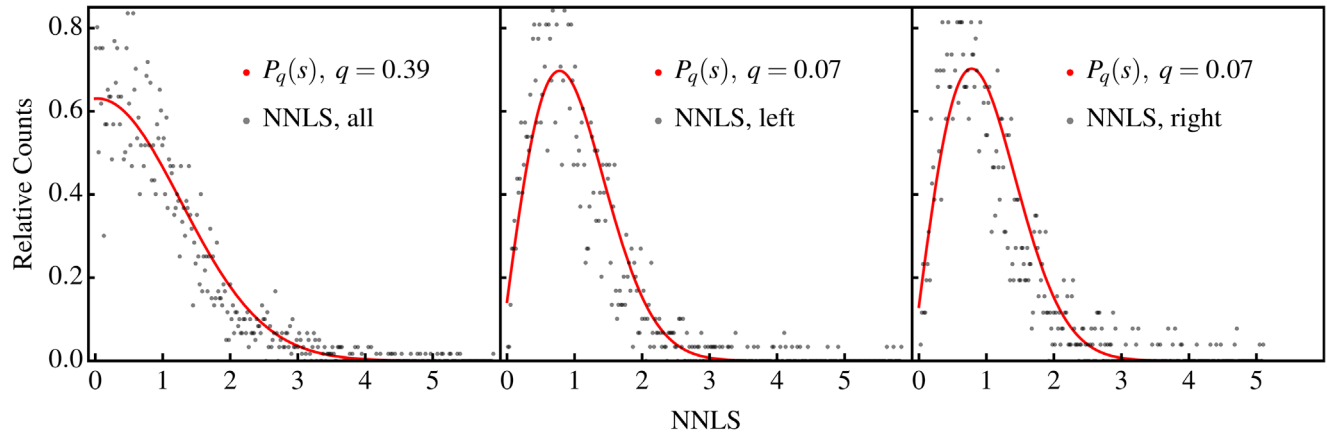TECHNOLOGIES**

www.advquantumtech.com

**Figure 3.** NNLS distributions of the double QD system (left panel), left QD (middle panel), and right QD (right panel). The parameter $q$ follows from fitting the calculated data to Equation (7). The centers of the QDs are 580 nm apart, leading to the localization of the first 3050 (energies ranging from 0.2 to 9 meV) states to either side. 500 impurities with $M = 0.65$ meV and $\sigma = 5.3$ nm are randomly dispersed across the two QDs.

The parameter $\nu$ connects between different common distributions, for instance $\nu = 0$ corresponds to the Poissonian, and $\nu = 1$ to the Gaussian orthogonal ensemble (GOE) of Wigner.[47] A further distribution proposed by Berry and Robnik[49] reads

$$
P_q(s) = e^{-qs}\left[q^2\mathrm{erfc}\left(\frac{\sqrt{\pi}}{2}\bar{q}s\right) + \left(2\bar{q}q + \frac{\pi}{2}\bar{q}^3 s\right)\exp\left(-\frac{\pi}{4}\bar{q}^2 s^2\right)\right],
$$
$$
\bar{q} = 1 - q
$$

(7)

where $s$ is normalized to the mean level spacing $\bar{s}$. A Poissonian (Wigner) distribution is obtained for $q = 1$ ($q = 0$). The *mixing parameter q* is a direct measure for the type of distribution signaling the coexistence of regular and chaotic behavior in the underlying classical phase-space.[47] Using Equation (7) to fit the NNLS obtained numerically provides a signature of the phase-space structure.

Another distribution with a quantum-mechanical background was presented by Izrailev,[48] where the NNLS distribution is approximated by the expression

$$
P_\beta(s) = As^\beta \exp\left(-\frac{\beta\pi^2}{16}s^2 - \left(C - \frac{\beta}{2}\right)\frac{\pi}{2}s\right),
$$
$$
1 = \int_0^\infty P(s)\mathrm{d}s,
$$
$$
1 = \int_0^\infty sP(s)\mathrm{d}s
$$

(8)

The parameters $A$ and $C$ are fixed by the normalization conditions, $0 \leq \beta \leq 2$, where for $\beta = 0$ this function reduces to the Poissonian distribution and for $\beta = 1, 2$ the GOE, Gaussian unitary ensemble (GUE) Wigner distributions[51] on a 5% (0.7%) confidence level, when the number of levels does not exceed $10^4$.[47,48] Hence, this distribution is well-suited to describe spin-orbit coupled systems or systems coupled to magnetic fields. We note that the mixing parameters are to be viewed only as a reasonable indi-

cator for quantum chaos without quantitative statements regarding the underlying phase space.

If not stated otherwise, the mixing parameters are obtained directly from the energy data. The complete spectrum is split according to the partial densities Equation (4) into energies belonging to states localized mostly in one of the QDs (left or right). The NNLS are obtained and normalized to the mean NNLS value. Then, the distributions Equations (6)–(8) are fitted to the respective normalized NNLS data. In this paper, the calculated eigenvalues are ordered by their magnitude and a histogram is calculated with $\Delta s = 0.02$, which corresponds to 0.55 μeV of the NNLS. Then, we fit Equations (6)–(8) to our data and extract the mixing parameters. If the QDs are effectively decoupled, the spectra are divided into two sub spectra containing only energies belonging to wave functions which are entirely localized in the left (right) QD. In the case where one QD is perturbed by impurities, the perturbed sub spectrum is expected to deviate from the Poissonian distribution while the unperturbed one remains (almost) unchanged (see **Figure 3**).

### 2.2.2. Identifying Scarred States

The number of scarred states cannot be determined by spectral measures. To calculate the scarred ratio, a base sample is selected which will be compared to the rest of the wave functions. Lower-energy as well as high-energy states (by means of the considered part of the spectrum) are selected because of the rapid oscillations and varying spacial extension. To find similar wave functions, the pre-selected sample of states will be compared to all other calculated states by applying a Gaussian filter $\mathcal{F}_\eta$ with a variance $\eta$ to remove the fast oscillations and calculating the mean squared error (MSE)

$$
d_{ij}^\eta = \sqrt{\mathrm{Mean}_{k,l}\left\{\left|\mathcal{F}_\eta\Psi_i(x_k, y_l) - \mathcal{F}_\eta\Psi_j(x_k, y_l)\right|^2\right\}}
$$

(9)

where the index $i$ counts through all obtained eigenstates and $j$ through the base-sample states. If not stated otherwise, $\eta$ is set to 190 nm for all calculations. When $i = j$ the matrix element is

**2200160 (4 of 12)**

**ADVANCED
SCIENCE NEWS**

www.advancedsciencenews.com

**ADVANCED
QUANTUM
TECHNOLOGIES**

www.advquantumtech.com

**Table 1.** Number of obtained states and the fraction of scarred states for a double QDs with centers spaced by 370 nm and having 198 impurities randomly distributed in $r(x + r_c, y) < 318$ nm, with $\sigma = 5.3$ nm and strengths ranging from $M = 0$ to 0.54 meV. The mixing parameter (Equation (7)) is shown for the whole (left, right) system. Typical scars are found throughout the whole spectrum and are shown in the last column. The pictures are convoluted with a Gaussian function with $\eta = 3.5$ using *scipy*'s *Gaussian_filter* function for better visibility.

| Impurity strength | Obtained states | % Scarred | Mixing $q$ | $(q_<, q_>)$ | Scars |
|---|---|---|---|---|---|
| 0 | 3032 | 9% | 1.0 | (1.0, 1.0) | |
| 54 μeV | 3053 | 26% | 1.0 | (1.0, 1.0) | |
| 0.14 meV | 3052 | 24% | 1.0 | (1.0, 1.0) | |
| 0.27 meV | 3007 | 21% | 1.0 | (1.0, 1.0) | |
| 0.41 meV | 3042 | 32% | 0.57 | (1.0, 0.43) | |
| 0.54 meV | 3035 | 29% | 0.39 | (0.53, 0.26) | |

zero. If $\Psi_i(x_k, y_l) \simeq \Psi_j(x_k, y_l)$ for all $k$, $l$, then $d_{ij} \ll 1$ and the states are considered similar. Every column of the matrix $\mathbf{d} \equiv d_{ij}^\eta$ is filtered with the mask $d_{ij} > \mu_j^{\mathrm{MSE}} - \sqrt{2}\sigma_j^{\mathrm{MSE}}$, where $\mu_j^{\mathrm{MSE}}, \sigma_j^{\mathrm{MSE}}$ are the mean and the variance of the respective column. The result is a matrix $\tilde{\mathbf{d}}$, where every non-zero entry represents a pair of highly similar states. This is a tedious task, which could be further automated by using an image classification algorithm using the *tensorflow* package. For similar systems (without external fields, equal shifts only varying the impurities) we found a good agreement with the MSE-approach. However, for this approach a preselected and classified large training data set is needed. Hence for the spin-less and SOC case different models are needed as well as for different magnetic fields, since those change the scar patterns which we are looking for.

### 2.3. Numerical Details

Eigenstates and eigenvalues are obtained by applying a third order finite central difference scheme to Equation (1) and solving the eigenvalue problem utilizing the *petsc4py* library. A Krylov-subspace method[52] was used with automatic parameter estimation from the package and a convergence measure of $10^{-12}$. Further, we ensured convergence by increasing the number of grid points of the finite differences. Since the calculations presented in this paper are quite time- and storage consuming, the order of wavefunctions might change using other methods but the statistics and the overall results remain valid.

## 3. Results

### 3.1. Influence of Coupling

Geometrical scarring can be observed for $r_c \geq 132$ nm in the energy range, where wavefunction tunneling according to Equa-

tion (5) is feasible. For smaller spacings, the shape of an individual QD is deformed such that, no typical scar (cf. **Table 1**) can be formed. In those cases, bouncing ball scars dominate the scarred wavefunction spectrum. For values $\geq 290$ nm, the tunnel barrier $V_B$ has reached the value $V_0$. Further, this mechanism can be viewed as an additional control parameter to enhance scarring at a certain energy assumed that the system is perfectly symmetric. In reality, this would not be the case. The influence of those imperfections is modeled by symmetry-breaking perturbations. Asymmetric perturbation is achieved by placing impurities inside the right QD, $x_{\mathrm{Imp}} > 0$, near its center (away from the tunnel barrier). The question is whether scars are formed and localized in the unperturbed (left) QD.

#### 3.1.1. Full Perturbation

For a QDs center distance of 580 nm we calculated the first 3050 eigenstates and found that all are fully localized in either QD. 500 impurities are randomly distributed in both QDs with an individual strength of $M = 0.65$ meV and $\sigma = 5.3$ nm. On both sides, we find 5-point star-like scars such as those in **Figure 4** but also straight paths (bouncing ball states). The statistical parameter derived from Equation (7) shows, that the whole system, as well as the subsystems, are in the strong scarring regime. In this case the statistics of the system and the two subsystems behave similar. This is to be expected since both subsystems are equally perturbed, leading to scarring. The values are $q = 0.39 \pm 2.6 \times 10^{-4}$ (all), $q = 0.074 \pm 1.6 \times 10^{-4}$ (left subsystem) and $q = 0.067 \pm 1.9 \times 10^{-4}$ (right subsystem) for in total 3050 data points ("all") and 1525 data points ("left" and "right"), see Figure 3 for zero magnetic field. Hence, the difference between the whole spectrum and the subsystems' spectra are not numerical errors. We observe that levels with small energy spacings are most affected by combining the subsystems. The perturbations shift the two sub spectra with respect to each other but
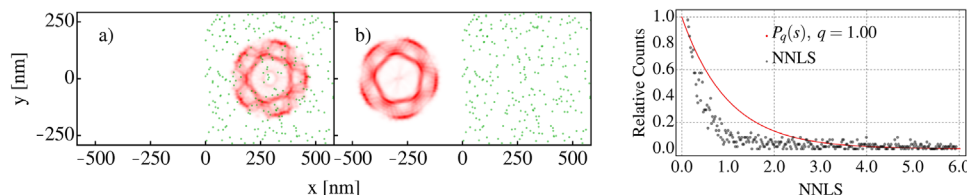
**Figure 4.** 5-Point star scars in the a) right and b) left QD, QDs separated by 580 nm, the tunnel barrier lies at $V_B = V_0 = 68.5$ meV. The impurities with ($M = 0.65$ meV, $\sigma = 5.3$ nm, cf. Equation (2)) located in the right QD are marked green. The 2746th (6.3 meV) and 1909th (8.1 meV) state are shown. c) The NNLS distribution of 3036 obtained eigenvalues.

do not lead to a strong level repulsion. These small energy-level spacings are thus ruled out by analyzing the symmetry-resolved spectra leading to a lower mixing parameter $q$, thus revealing the perturbation induced level repulsion in each QD.

### 3.1.2. Partial Perturbation

When all impurities are in the right QD, strong localization and prominent scars on both QDs are still observed. Two examples are shown in Figure 4, where 261 Gaussian impurities with $\sigma = 5.3$ nm and $M = 0.65$ meV are added only to the right QD (i.e., at $x > 0$). Even if the strength is lowered to $M = 7$ μeV, all states are fully located either in the left or the right QD. Moreover, the impurities lead to dynamical scarring. Prominent scars are visible similar to those reported in ref. [#0028] for a single QD. The star-shaped scars are found in both QDs, the perturbed and the unperturbed one, although, the QDs couple only weakly. This seems to be counter intuitive. Both, the left and right QD wave functions have (when considered separately) an exponentially decaying tail into the other subsystem, which is obviously sufficient to trigger the formation of scars in an unperturbed region which for itself does not host scars. We call such scars phantom scars. The non-linearity of the left QD potential is not necessary for the scar formation. Using a harmonic potential for the left QD, scars are also formed (results not shown for brevity). We note here the difference to Anderson-localized modes[53,54] which are usually restricted to a perturbed region and less influenced by distant regions such as system boundaries. The appearance of phantom scars endorse the fact, that although scarring is limited to a very narrow frequency window, scars span the whole system signaling a quantum mechanical coherence between different parts of the system. For example, one may conduct experiment on the left QD only and evidence the presence of the phantom scars. Removing the impurities in the right QD switch off this dynamical scar state.

For a quantitative insight, Figure 4 shows the NNLS distribution for the lowest 3036 eigenstates. The mixing parameter $q = 1$ is inferred by fitting the distributions of NNLS to Equation (7). For impurity-assisted scarring a shift toward a Wigner distribution is expected, however, a Poissonian distribution was obtained. The same result is found when the sub spectra for the left and right subsystem are fitted to Equation (7). In contrast, the scars found in Figure 4 are not isolated features, similar states are found over the whole spectrum calculated for this analysis. The similarity analysis, with only star-shaped scars as basis, shows that almost 22% of the eigenfunctions are scarred. In con-

trast, the full perturbed system shows around 6% scarred eigenfunctions, although the spectral statistics are hinting for much stronger scarring. However, it seems that the perturbation is too strong and the system is already in a regime where the impurities destroy the quantum scars. This is surprising, since the parameters for the impurities chosen for the full perturbed system are well suited for strong quantum scarring in a single $r^5$-QD.

The impurities located inside the tunnel barrier are likely the reason for scarring in the supposedly unperturbed system. To address this, the impurities were shifted toward the center of the right subsystem. Now, the impurities are placed in the area $r(x + r_c, y) < 318$ nm, the number of impurities is 198, $\sigma = 5.3$ nm and $M = 0.54$ meV. Again, scarred eigenfunctions are found both, in the left (unperturbed) and right (perturbed) QD, where around 29% of 3046 wave functions are scarred. The eigenfunctions are still completely localized either to the left or right subsystem. Thus, the unperturbed subsystem is still influenced by the perturbation and scars are formed even in the uncoupled regime. This finding is supported by the spectral statistics of the system. If all eigenvalues are considered, the NNLS distribution is purely Poissonian ($q = 0$), the same time both sub spectra for the left and right QD are in the strongly mixed phase ($q = 0.2$).

### 3.1.3. Strong Tunneling Regime

Figure 2 indicates that (for the first 3000 states we calculated) an inter-dot spacing below 370 nm allows for the formation of tunneling. We considered QDs with their centers spaced by 370 nm with 198 impurities within the area encircled by $r(x + r_c, y) < 318$ nm, with a strength $M = 0.4$ meV and $\sigma = 5.3$ nm. Only the lowest few hundred states are localized in either dots, all other wave functions are spread over the whole system. The spectral analysis of the NNLS shows that when interdot scattering is strong, the mixing parameter for the system is $q = 0.56$, indicating the possibility of strong quantum scarring. The sub spectra for the left and the right dots behave very differently. The right subsystem which is subjected to the perturbing potential has a mixing parameter $q = 0.43$, which is comparable to the one found for the whole system. However, the left subsystem shows Poissonian behavior ($q = 0$), where we expect the absence of scarring. In contrast to this finding, the typical scars which have been presented before are still found among the states strongly localized in the unperturbed QD.

Indeed, many of the eigenfunctions are scarred, but now a multitude of other classical paths are found. In **Figure 5** three different scarred wave functions are shown, namely the states 2765,

**2200160 (6 of 12)**

**ADVANCED
SCIENCE NEWS**

www.advancedsciencenews.com

**ADVANCED
QUANTUM
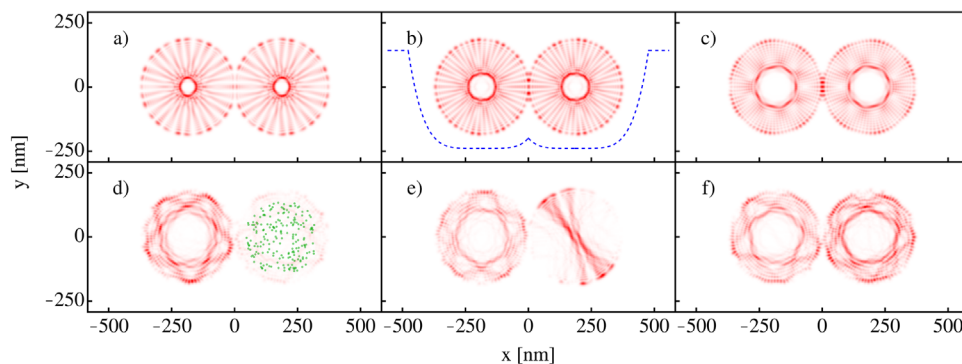TECHNOLOGIES**

www.advquantumtech.com

**Figure 5.** Double QDs with centers spaced by 370 nm and with 198 impurities with $\sigma = 5.3$ nm. Corresponding states with the same energies without (a–c) and with impurities (d–f with $M = 0.4$ meV) are shown. In panel (d), the location of the impurities used for panels (d–f) are denoted by green dots. Top: States 2809, 2813, and 2863 are shown with energies 8.25, 8.27, and 8.36 meV. The blue line in panel (b) indicates the cross-section of the potential at $y = 0$. The height of the potential at $x = 0$ is $V_B = 7.2$ meV. Bottom: 5-Point star scars in the left (d,e) and both (f) QDs. The state in panel (d) is strongly localized in the unperturbed QD but is still scarred. The 2765th, 2775th, and 2818th state are shown (corresponding energies 8.25, 8.26, and 8.35 meV). Previously unscarred states are scarred after adding impurities.

2775, and 2818 with eigenenergies 8.25, 8.27, and 8.35 meV. In total, around 31% of the calculated wave functions (total 3042 obtained) were scarred, see Figure 5 (not counting straight paths like panel b). This shows, that scarring in this system is very robust against coupling it to another system.

A relevant question concerns the stability of scarring against perturbation, that is, with increasing strength $M$ of the impurities. Scarring is destroyed for most systems calculated in this paper at impurity-strength above 0.65 meV. The results for the calculations of six different impurity strengths (0, 54 μeV, 0.14 meV, 0.27 meV, 0.41 meV, 0.54 meV) are shown in Table 1 along with their spectral statistics obtained from fitting the NNLS to Equation (7). In all calculations typical scars are found. Surprisingly, this is not supported by the spectral statistics. When impurities are present, in every system more than 20% of the calculated states were scarred, but the spectral analysis predicts no scarring. At least none, which are purely impurity-assisted. When no impurities are placed inside the right subsystem ($M = 0$), around 9% of the states were scarred. The true number for all considered configurations is even higher, when bouncing-ball scars are considered as well. However, most scars are present in the high-energy regime, while in the other cases already the first few hundred states may show scar features.

The geometry of the system favors inherently the formation of scars which are only found when perturbing a single QD. When both QDs are decoupled, no scars are found, but when the system is moved into the coupling regime, individual and coupled scars emerge. This also happens without impurities. Table 1 shows, that this process is strongly enhanced, when the system is perturbed. In this case, it is of no relevance where the perturbations are placed, it is already enough when only one subsystem is subjected to impurities.

For the configurations presented in Table 1 the enhancement of scarring is largest at a strength of $M = 0.41$ meV with around 3.5 times more scars. This is accompanied by an increase of oscillations away from the classical path. Also, when the QDs are coupled, the 5-point stars tend to align with each other. They either touch in one corner or in two corners, see Table 1 ($M = 0$). In a single QD the orientation of the path is quite random, the

scar maximizes the overlap with impurities but our calculations showed that multiple orientations are found nonetheless. This makes the configuration presented here interesting for transport applications since the orientation of scars is deterministic due to the geometry.

### 3.2. Magnetic Fields and (Local) Spin-Orbit Coupling

For an applied magnetic field $\mathbf{B} = B_0\mathbf{e}_z$ we use the symmetric gauge $\mathbf{A} = B_0/2(-y, x, 0)$. The field strength $B_0$ varies from 0 to 0.94 T. The magnetic field leads to a deflection of the charge carriers resulting in new short periodic orbits. For a magnetic field strength $B_0 = 0.7$ T we find elliptical, triangular, and deformed five-point-structured scars. Performing calculations of the corresponding classical billiard reveal these periodic orbits in the classical case as well.

Without impurities and magnetic field ($M = 0$, $B_0 = 0$), the system is left/right symmetric with respect to $y = 0$. When a magnetic field is applied, the system is point-symmetric around the origin. Overall, the partial densities show the same features as without magnetic field, uncoupled and coupled regimes exist depending on the distance of the QDs and the energy of the considered eigenstates. Due to the vector potential, particles will be deflected in different directions in each QD. Hence, the individual QDs have the same energy-spectra but the wave functions have different phases, which can lead to a localization to either QD in the uncoupled regime, even without impurities. The analysis of the NNLS for each system are shown in **Figure 6**. the magnetic field strength varies from 0 to 0.94 T in steps of 4.7 mT. The qualitative behavior for a half-perturbed system in dependence on impurity strength and magnetic field is well captured qualitatively for the whole, as well as for the sub spectra, no matter which fit-model (Equations (6)–(8)) was used. For these calculations 198 impurities were scattered in the right QD (see Figure 5d). With increasing impurity strength $M$, the statistical parameters hint for increasing chaoticity in the system. However, we observe a jump within all statistical models (Figure 6) when the magnetic field is switched on. This could be due to the lifted degeneracy, shift-
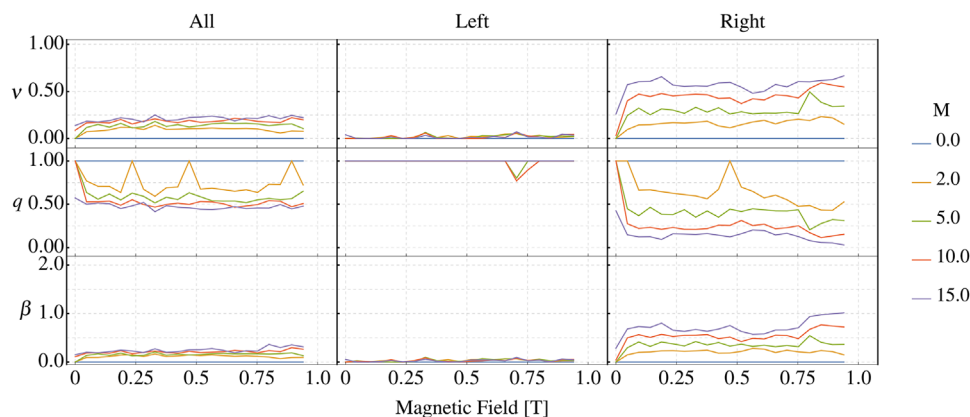
**ADVANCED
SCIENCE NEWS**

www.advancedsciencenews.com

**ADVANCED
QUANTUM
TECHNOLOGIES**

www.advquantumtech.com

**Figure 6.** Fitting values of all considered distributions, see Equations (6)–(8), of a half-perturbed system with $r_c = 185$ nm without SOC ($\alpha = 0$). In total 3000 eigenvalues were calculated and the spectra for the whole (all), left and right QDs were investigated. Note the larger $\gamma$-range for the Izrailev-parameter $\beta$. In all cases, the deviation from the Poissonian distribution of spectra belonging to the right subsystem increases with increasing impurity strength. The left unperturbed QD is in all cases almost Poissonian ($q = 0$, $\nu = 0$, $\beta = 1$). For the spectra of the whole system, the strongest deviations occur for the Berry–Robnik–Izrailev-distributions. These models occur to be more sensitive to impurity-induced perturbation. However, the qualitative behavior is well captured by all models.
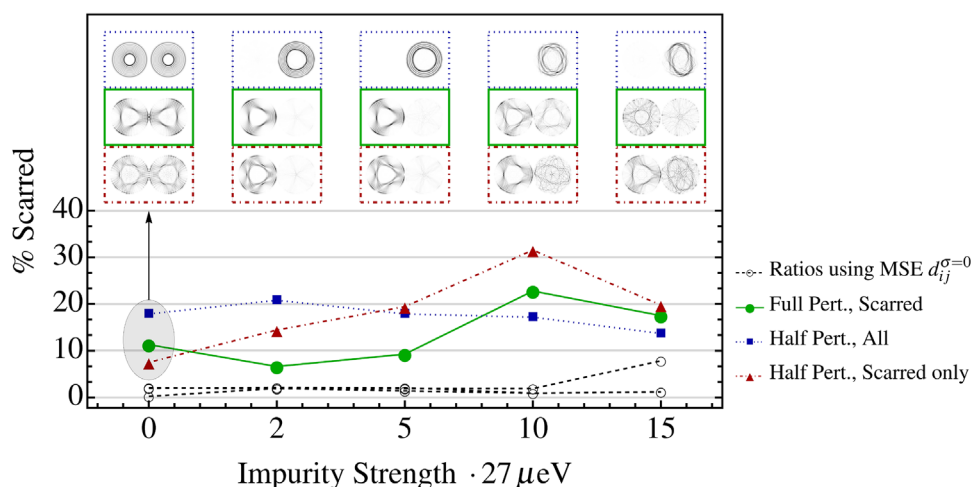


**Figure 7.** Ratio of scarred states of a full perturbed and half perturbed system with a QDs centers spacing of 370 nm, a magnetic field strength of 700 mT and three corresponding examples of the examined eigenstates for each perturbation. Black curves show the similarity ratios when the MSE $d_{ij}$ is calculated without Gaussian smoothing ($\sigma = 0$). Other data points are the mean value of the MSE for $\eta = 130$ and 190 nm. Without smoothing, Equation (9) provides no reliable results due to short wavelength oscillations of the wave functions. Scars in the unperturbed case ($M = 0$) remain scarred (blue curve), while new scarred states emerge with increasing impurity strength (red and green curves). With strong perturbations ($M > 0.4$ meV), scars are destroyed. Note the matching color of the frame of each eigenstate. Around 3000 states were calculated for each configuration.

ing smaller values in the NNLS to the right part of the spectrum, leading to stronger deviations from the Poissonian distribution.

In line with the findings for the field-free case, a strong increase in the number of scarred eigenstates is observed when an external magnetic field is applied. Some results for a fully perturbed and half perturbed system with a separation of the QDs of 370 nm and a magnetic field of 700 mT are shown in **Figure 7**. There, the MSE (Equation (9)) was calculated for selected states which are scarred in systems without impurities (green, fully perturbed and blue, half perturbed). Unscarred states in a system without impurities transform into scars when impurities are added, even when they are solely located in the right subsystem. A typical example is shown in the top row (blue framed states)

of Figure 7. Without impurities the state can be represented as a sum of independent unperturbed eigenfunctions of a single QD. When the perturbation becomes stronger, an elliptical scar in the perturbed region forms. In total, this increases the number of scarred eigenstates in the spectrum. We observe a peak of the ratio of scarred states at around 20% to 30% for the fully perturbed and the half perturbed system, which supports our findings in the field-free case. With even stronger perturbation, the wave functions become more chaotic, as exhibited by the wave functions in Figure 7 for $M = 0.27$ and 0.4 meV. Also, the fixed orientation (see the green framed state at $M = 0$ of Figure 7) which was previously found in the field-free case is destroyed in the limit of strong perturbation. This state splits up into partial scars in
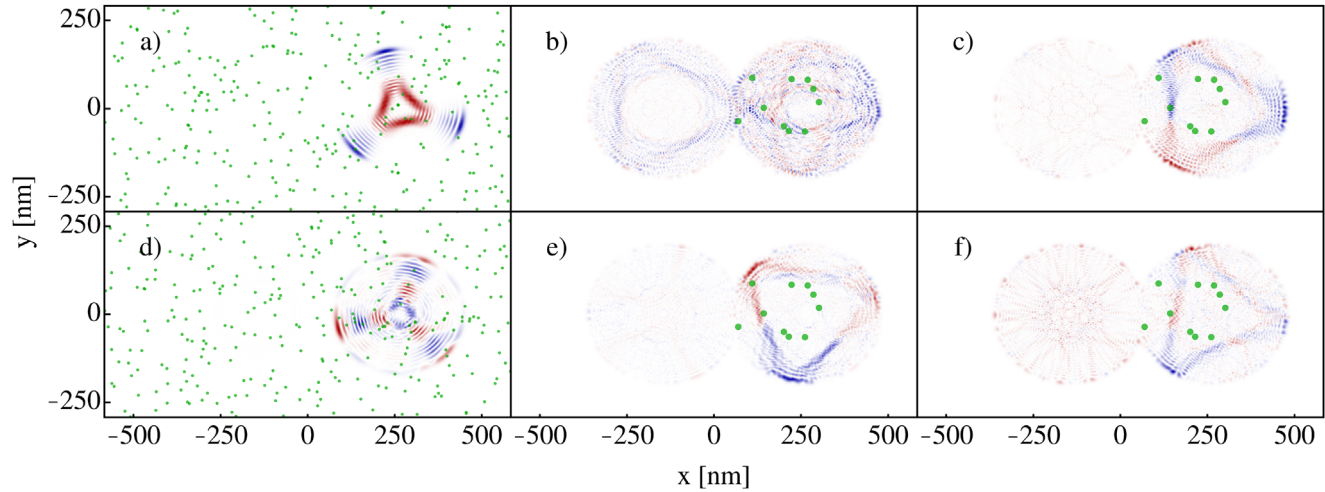
**ADVANCED**
**SCIENCE NEWS**

www.advancedsciencenews.com

**ADVANCED**
**QUANTUM**
**TECHNOLOGIES**

www.advquantumtech.com

**Figure 8.** Spin density $s_z(r)$ for the states 2886 a) with $\alpha = 7\,\text{meV}\AA$ and 2768 d) with $\alpha = 22\,\text{meV}\AA$. Double QDs centers are spaced by 370 nm. 198 impurities are present in the right QD with $\sigma = 5.3$ nm. Magnetic field strength is $B_0 = 940$ mT. Spin density $s_z(r)$ with local Rashba impurities (Equation (11)), QDs centers are spaced by 370 nm, and ten impurities with $\sigma = 5.3$ nm were added. Magnetic field strength is $B_0 = 700$ mT and the SOC strength is $\alpha = 14, 22, 29, 36\,\text{meV}\AA$ (b,c,e,f).

the right and the left QDs when impurities are present. Figure 7 shows only the scar, where the density shifts toward the unperturbed subsystem.

Spin-orbit coupling roughly doubles the number of wave functions needed to cover the same energy range compared to the spin-less case. We rely on parameters found from previous calculations to identify scarred eigenstates. Without SOC (i. e., $\alpha = 0$), the spin-up and -down states are energetically degenerate. For weak SOC, a dominant contribution to the distribution of the NNLS near $s = 0$ arises. For an insight it is beneficial to analyze the spin-resolved spectra.[44,55] Here, the magnetic field was varied from 60 to 940 mT, and three values for the SOC parameter $\alpha$ were chosen, $7, 14$, and 22 meVÅ. Even with SOC, scars are found. Typical examples are shown in **Figure 8** where the spinor-components are shown in the first two columns ($\bar{\Psi} = (\Psi_\uparrow, \Psi_\downarrow)$) and the third column shows the local spin density

$$s_z(r) = |\Psi_\uparrow(r)|^2 - |\Psi_\downarrow(r)|^2 \tag{10}$$

The Rashba SOC couples the components of the spin with the kinetic momentum by the terms $\sigma_x p_y$ and $\sigma_y p_x$. A large contribution of these terms is expected at regions where the momentum vector changes its direction. This can be observed in Figure 8 (third column), where a flip in the $z$-component is visible at the corners of the trajectory or regions with strong curvature. In contrast, radially symmetric wave function have spatially separated spin paths, that is, $\Psi_\uparrow$ concentrates around a circle of radius $r_\uparrow$ and $\Psi_\downarrow$ around $r_\downarrow$. In the case with localized SOC, we assume a local enhancement of the SOC parameter. Hence, the SOC part of Equation (1) changes to

$$H_{\text{LSOC}} = \left( \alpha \sum_{n=1}^{N_{\text{Imp}}} V_{\text{Imp}}(r_n) \right) (\boldsymbol{\sigma} \times \boldsymbol{\Pi})_z \tag{11}$$

where the impurities represent localized SOC. Further, we assume that the local coupling is dominating. Hence, a strong

change in the local spin density is expected at the impurity locations while, for example, the $s_z$ component is constant away from the perturbing potential. This can be seen in the second and third column of Figure 8, where in contrast to conventional SOC spin flip (color change from blue to red or vice versa) occurs in regions, where only a small change in the momentum is expected.

### 3.3. Correlators and Wavepacket Dynamics

Next, we computed the correlators of the form

$$C(\mathcal{E}_i, \mathcal{E}_j)_d = \mathcal{E}_i(\tilde{r})\mathcal{E}_j(\tilde{r} + d) - \mathcal{E}_j(\tilde{r})\mathcal{E}_i(\tilde{r} + d) \tag{12}$$

where $\tilde{r}$ ($0 \leq \tilde{r} \leq 1$) is the arc length measured along the scar trajectory and $d$ is the shift, $0 \leq d \leq 1$ and $\mathcal{E}_{i,j}(\tilde{r})$ are expectation values of any operator along the trajectory. Here, $d = 1$ represents a full rotation of the trajectory, $d = 0.5$ is a half shift (in case of a circle it is a 180° rotation). Hence, the function $C(\sigma_x, \sigma_y)$ is symmetric to the point $d = 0.5$. Some examples are shown in **Figure 9**, where the correlation between the $x$- and $y$-components of the spin expectation (Equation (12)) value along various trajectories are shown. In most cases, the correlator has random oscillations which might be connected to strong local density oscillations of the state along the trajectory. The purity of the scar has a strong influence on the correlator, leading to increased correlation by orders of magnitude for isolated states (Figure 9a (green curve), Figure 9c (yellow curve)). Therefore, we expect a vanishing effect of correlation of any observable due to scars in the weak scarring regime, namely when a small fraction of states is scarred.

The wavepacket dynamics in a system with local SOC was investigated. Previous studies indicated clear recurrence features for single-particle as well as for the many-body dynamics.[20,28,56,57] Here, a wavepacket is launched along the scar, that is, an electron is injected into the nanostructure, for
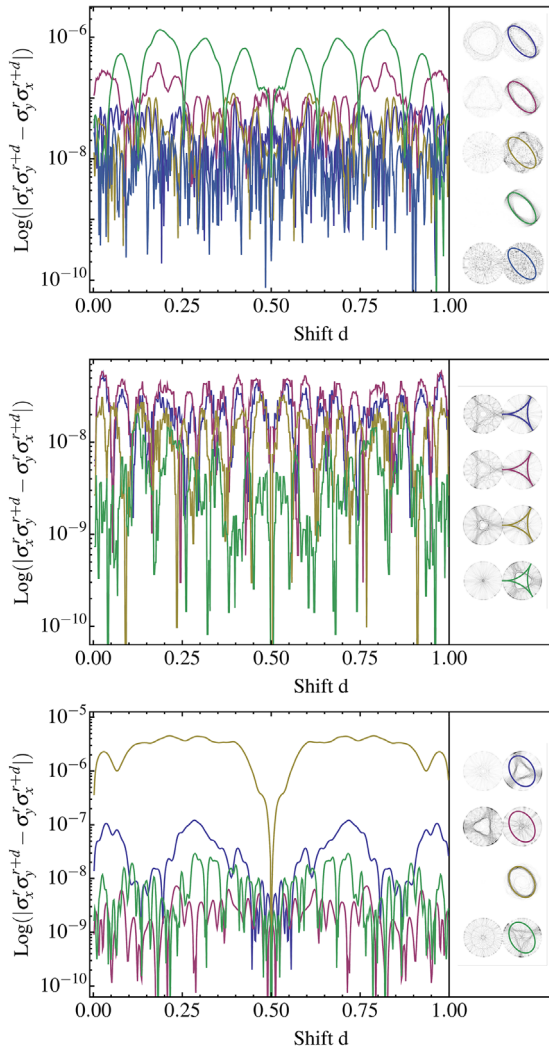
**ADVANCED
SCIENCE NEWS**

www.advancedsciencenews.com

**ADVANCED
QUANTUM
TECHNOLOGIES**

www.advquantumtech.com

**Figure 9.** Spin-expectation value correlator $C(\sigma_x, \sigma_y)$ (Equation (12)) for a system with local SOC (left panel, $B_0 = 700$ mT, $\alpha = 14$ meV∀, $N_{Imp} = 10$) and magnetic impurities ($B = 940$ mT, $N_{Imp} = 197$, $\alpha = 7$ (middle) and 14 meV∀ (right)). Note the logarithmic scale. $d$ denotes the shift of the oberservables along the path (1 corresponds to a shift amounting to the full path length).

a system with ten impurities acting as a source of local SOC (see Equation (11)). We calculated the fidelity $F(t)$ with respect to the initial state, the overlap $O_{Imp}$ of the wavepacket with the impurity potential and the expectation value of the $s_z$ component. We defined the fidelity and overlap as

$$F(t) = \left| \iint \Psi(0)\Psi^*(t) \mathrm{d}x\,\mathrm{d}y \right|^2$$

$$O_{Imp}(t) = \sum_{n=1}^{N_{Imp}} \iint \left( \frac{|\Psi^\uparrow(t)|^2 V_{Imp}(r_n)}{\varepsilon + |\Psi^\uparrow(0)|^2 V_{Imp}(r_n)} + \frac{|\Psi^\downarrow(t)|^2 V_{Imp}(r_n)}{\varepsilon + |\Psi^\downarrow(0)|^2 V_{Imp}(r_n)} \right) \mathrm{d}x\,\mathrm{d}y$$

$$(13)$$

where $\Psi(t) = (\Psi^\uparrow(t), \Psi^\downarrow(t))$ denotes the spinor at time $t$ and $\varepsilon$ is a real positive number to ensure convergence in case the denominator equals zero. Here, we used a value of $\varepsilon = 10^{-2}$. In **Figure 10**, the fidelity, the impurity overlap, and $\sigma_z$ expectation value are plotted for a wavepacket launched on the scar of Figure 8 (top row, last column) at $r_0 = (76, -37)$ nm, with momentum $p = (4.37, -1.6)$ meV$^{1/2}$. Cases with two FWHMs along the scar of 120 and 250 nm and a perpendicular FWHM of 12 nm were considered, with similar results for the time propagation. The scarred state has an expectation value $s_z = 4 \times 10^{-2}$, it is almost unpolarized in total, while the local spin density fluctuates along the trajectory. Flips of the local density are observable near the SOC impurities, in the upper right part of Figure 8 the separation of the spin-up and spin-down trajectories are observed. Five resonances of the fidelity are clearly visible, where after $T_1 = 20$ ps only 10% to 20% of the wavepacket coincide with its initial form. The first recurrence time $T_1$ varies from 19.3 ps ($s_z(0) = -1$) to 19.8 ps ($s_z(0) = 1$). Apparently, the wavepacket is slowed down depending on its preparation state, but the influence is still minor compared to the total propagation time. Also the value $F(T_1)$ depends on the initial spin polarization of the wavepacket. The strongest recurrence is observed, when its total polarization equals +1. However, the initial polarization is destroyed after about 10 ps for all considered cases. This time is exactly when the overlap $O_{Imp}(t)$ maximizes for the first time. Due to the local SOC, the polarization state of the wavepacket is destroyed and starts to fluctuate with a frequency of about 20 ps, which matches the recurrence time $T_1$.

## 4. Summary and Discussion

We studied the impact of scalar and magnetic perturbations on the carrier dynamics in double quantum dots subject to external fields and Rashba-type SOC. We find two types of quantum scarring, geometrical and perturbation-induced scarring. Different regimes were identified, where the subsystems are effectively decoupled or tunneling is significant; these regimes are quantified on the basis of partial densities. Analyzing the spectra evidences the mixed nature of the phase space for a large number of geometries and fields. Numerous types of quantum scars are identified. A partial perturbation leads to scars in the unperturbed subsystem even in the weak tunneling regime. Geometrical scars formed even without impurities proved to be stable against strong perturbations. The fraction of scarred wave functions could be enhanced by perturbation up to a factor of three. The wavepacket recurrence is studied. Recurrence persists for rather strong SOC and perturbations caused by locally varying SOC. The results illustrate the versatile nature of scarring and also the difference of quantum scarring to other localization phenomena such as Anderson and weak localization.[53,54] The latter occurs usually at low frequencies whereas scarring emerges at high frequencies. In addition, Anderson-localized modes are basically restricted to subregion and are less affected by details of remote regions (such as boundary details or distant inhomogeneities). As demonstrated by the phantom scars, scarring occurs in a narrow frequency window but is a global phenomena spanning the whole system domain and depends on a coherent interplay between far separated regions including their boundaries. For in-
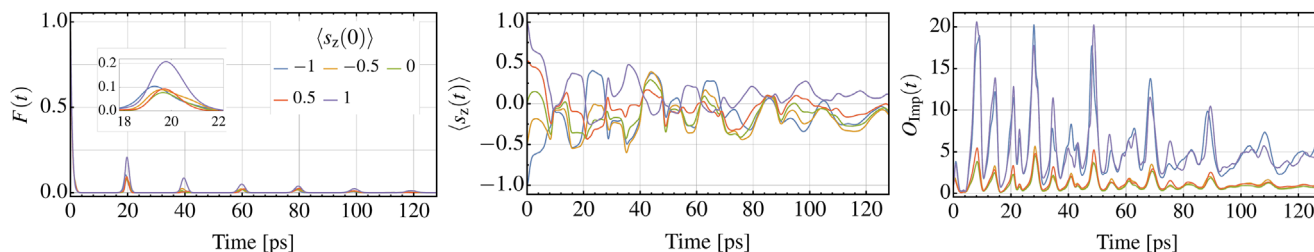
**ADVANCED
SCIENCE NEWS**

www.advancedsciencenews.com

**ADVANCED
QUANTUM
TECHNOLOGIES**

www.advquantumtech.com

**Figure 10.** Fidelity $F(t)$, $s_z$ expectation value and perturbation potential overlap $O_{Imp}(t)$ (Equation (13)) of a wavepacket launched on the scar of Figure 8 (top row, last column) with five different spin-polarizations. The fidelity shows recurrences at multiples of about 20 ps (inset shows peak at 20 ps) up to 100 ps, where the wavepacket is fully delocalized. At 10 ps, the interaction with the perturbing potential has drastically increased rendering the expectation value of the $z$-component of the spin dropping (increasing).

stance, a change of the impurity configuration in a scarred QD affects directly the phantom scar in another quantum dot.

## Conflict of Interest

The authors declare no conflict of interest.

## Data Availability Statement

The data that support the findings of this study are available from the corresponding author upon reasonable request.

[1] F. Haake, M. Kús, P. Seba, H.-J. Stöckmann, U. Stoffregen, *J. Phys. A: Math. Gen.* **1996**, *29*, 5745.

[2] M. Tomiya, N. Yoshinaga, *J. Stat. Phys.* **1996**, *83*, 215.

[3] A. Csordas, J. Cserti, A. Pályi, U. Zülicke, *Eur. Phys. J. B* **2006**, *54*, 189.

[4] P. O'Connor, J. Gehlen, E. J. Heller, *Phys. Rev. Lett.* **1987**, *58*, 1296.

[5] A. Bäcker, R. Schubert, *J. Phys. A: Math. Gen.* **2002**, *35*, 527.

[6] S. W. McDonald, *Wave Dynamics of Regular and Chaotic Rays*, California University, Berkeley, Lawrence Berkeley Lab **1983**.

[7] E. J. Heller, *Phys. Rev. Lett.* **1984**, *53*, 1515.

[8] E. J. Heller, *The Semiclassical Way to Dynamics and Spectroscopy*, Princeton University Press, Princeton, NJ **2018**.

[9] W. Li, L. E. Reichl, B. Wu, *Phys. Rev. E* **2002**, *65*, 5.

[10] Generally, quantum states of a system with classically chaotic dynamics are expected to behave locally as a random superposition of plane waves (in contrast to scars)[11].

[11] M. V. Berry, *Chaotic Behaviour of Deterministic Systems* (Ed: A. Chenciner), Vol. *36*, North-Holland, Amsterdam **1983**.

[12] Effects of geometric scarring on physical observables are in general weak (unless the observable in question is affected only by scarring) since the part of the corresponding phase space diminishes for $\hbar \to 0$ and the dynamics is basically ergodic.

[13] B. Eckhardt, *Phys. Rep.* **1988**, *163*, 4.

[14] E. B. Bogomolny, *Phys. D* **1988**, *31*, 169.

[15] M. V. Berry, *Proc. R. Soc. London, Ser. A* **1989**, *423*, 219.

[16] S. Sridhar, *Phys. Rev. Lett.* **1991**, *67*, 785.

[17] J. Stein, H.-J. Stöckmann, *Phys. Rev. lett.* **1992**, *68*, 2867.

[18] W. Li, L. E. Reichl, B. Wu, *Phys. Rev. E* **2002**, *65*, 056220.

[19] T. Prosen, *J. Phys. A: Math. Gen.* **1998**, *31*, 7023.

[20] J. Keski-Rahkonen, P. J. J. Luukko, S. Aberg, E. Räsänen, *J. Phys.: Condens. Matter* **2019**, *31*, 105301.

[21] J. Keski-Rahkonen, A. Ruhanen, E. J. Heller, E. Räsänen, *Phys. Rev. Lett.* **2019**, *123*, 214101.

[22] I. V. Zozoulenko, K.-F. Berggren, *Phys. Rev. B* **1997**, *56*, 6931.

[23] L. Huang, Y.-C. Lai, D. K. Ferry, S. M. Goodnick, R. Akis, *Phys. Rev. Lett.* **2009**, *103*, 054101.

[24] L. Huang, Y.-C. Lai, D. K. Ferry, R. Akis, S. M. Goodnick, *J. Phys.: Condens. Matter* **2009**, *21*, 344203.

[25] L. Ying, L. Huang, Y.-C. Lai, C. Grebogi, *Phys. Rev. B* **2012**, *85*, 245448.

[26] D. Cabosart, A. Felten, N. Reckinger, A. Iordanescu, S. Toussaint, S. Faniel, B. Hackens, *Nano Lett.* **2017**, *17*, 1344.

[27] G. Q. Zhang, X. Chen, L. Lin, H. Peng, Z. Liu, L. Huang, N. Kang, H. Q. Xu, *Phys. Rev. B* **2020**, *101*, 085404.

[28] P. Luukko, B. Drury, A. Klales, L. Kaplan, E. J. Heller, E. Räsänen, *Sci. Rep.* **2016**, *6*, 37656.

[29] J. Keski-Rahkonen, P. J. J. Luukko, L. Kaplan, E. J. Heller, E. Räsänen, *Phys. Rev. B* **2017**, *96*, 094204.

[30] C. J. Turner, A. Michailidis, D. A. Abanin, M. Serbyn, Z. Papi, *Nat. Phys.* **2018**, *14*, 745.

[31] M. Schecter, T. Iadecola, *Phys. Rev. Lett.* **2019**, *123*, 147201.

[32] D. K. Mark, C.-J. Lin, O. I. I. Motrunich, *Phys. Rev. B* **2020**, *101*, 195131.

[33] S. Chattopadhyay, H. Pichler, M. D. Lukin, W. W. Ho, *Phys. Rev. B* **2020**, *101*, 174308.

[34] K. Pakrouski, P. N. Pallegar, F. K. Popov, I. R. Klebanov, *Phys. Rev. Lett.* **2020**, *125*, 230602.

[35] L. Zhang, B. Zhao, T. Devakul, D. A. Huse, *Phys. Rev. B* **2016**, *93*, 224201.

[36] D. J. Luitz, N. Laflorencie, F. Alet, *Phys. Rev. B* **2015**, *91*, 081103(R).

[37] R. Vasseur, A. J. Friedman, S. A. Parameswaran, A. C. Potter, *Phys. Rev. B* **2016**, *93*, 134207.

[38] J. A. Kjäll, J. H. Bardarson, F. Pollmann, *Phys. Rev. Lett.* **2014**, *113*, 107204.

[39] M. Serbyn, J. E. Moore, *Phys. Rev. B* **2016**, *93*, 041424(R).

[40] For an overview we refer to the topical issue *Many-Body Localization*, (Ed: J. H. Bardarson et al.), Ann. Phys., **2017**.

[41] V. Oganesyan, A. Pal, D. A. Huse, *Phys. Rev. B* **2009**, *80*, 115104.

[42] M. Azimi, M. Sekania, S. K. Mishra, L. Chotorlishvili, Z. Toklikishvili, J. Berakdar, *Phys. Rev. B* **2016**, *94*, 064423.

[43] V. K. Dugaev, J. Barnas, J. Berakdar, *J. Phys. A: Math. Gen.* **2003**, *36*, 9263.

[44] M. Berger, D. Schulz, J. Berakdar, *Nanomaterials* **2021**, *11*, 5.

[45] A. Dyrdał, J. Barnas, V. K. Dugaev, J. Berakdar, *Phys. Rev. B* **2018**, *98*, 075307.

[46] A. Grant, J. Rosner, *Am. J. Phys.* **1994**, *62*, 310.

[47] H. Stöckmann, *Quantum Chaos: An Introduction*, Cambridge University Press, Cambridge **1999**.

[48] F. M. Izrailev, *Phys. Lett. A* **1988**, *134*, 13.

[49] M. V. Berry, M. Robnik, *J. Phys. A: Math. Gen.* **1984**, *17*, 2413.

[50] T. A. Brody, *Lett. Nuovo Cimento* **1973**, *7*, 482.

[51] H. Silberbauer, P. Rotter, U. Rössler, M. Suhrke, *Europhys. Lett.* **1995**, *31*, 7.

[52] V. Hernandez, J. E. Roman, V. Vidal, *ACM Trans. Math. Software* **2005**, *31*, 3.

[53] P. W. Anderson, *Phys. Rev.* **1958**, *109*, 1492.

[54] D. J. Thouless, *Phys. Rep.* **1974**, *13*, 93.

[55] O. V. Marchukov, A. G. Volosniev, D. V. Fedorov, A. S. Jensen, N. T. Zinner, *J. Phys. B: At., Mol. Opt. Phys.* **2014**, *47*, 195303.

[56] W. Ho, S. Choi, H. Pichler, M. D. Lukin, *Phys. Rev. Lett.* **2019**, *122*, 040603.

[57] C. Turner, A. Michailidis, D. Abanin, M. Serbyn, Z. Papic, *Nat. Phys.* **2018**, *14*, 745.